ADVANCED FUNCTIONAL MATERIALS
www.afm-journal.de

www.MaterialsViews.com

Highly Conductive, Bendable, Embedded Ag Nanoparticle Wire Arrays Via Convective Self-Assembly: Hybridization into Ag Nanowire Transparent Conductors

Dong Yun Choi, Yong Suk Oh, Donggeon Han, Seunghyup Yoo, Hyung Jin Sung, and Sang Soo Kim**

The optoelectrical properties of Ag nanowire (NW) networks are improved by incorporating the NWs into highly conductive ordered arrays of Ag nanoparticle wires (NPWs) fabricated via surfactant-assisted convective self-assembly. The NPW–NW hybrid conductor displays a transmittance (T) of 90% at 550 nm and a sheet resistance (R_s) of 5.7 Ω sq^{-1}, which is superior to the corresponding properties of the NW network showing a R_s of 14.1 Ω sq^{-1} at a similar T. By the modified wettability of a donor substrate and the capillarity of water, the sintered NPW–NW hybrid conductors are perfectly transferred onto an UV-curable photopolymer film, and the embedded hybrid conductors exhibit excellent electromechanical properties. The R_s and T of the NPW arrays can be predicted by using a simple model developed to calculate the width and height of the hexagonal close-packed particles formed during the convective self-assembly. The numerical analysis reveals that the maximum Haacke figure of merit of the NW networks is increased considerably from 0.0260 to 0.0407 Ω^{-1} by integration with the NPW array. The highly conductive NPW arrays generated using a simple, low-cost, and nonlithographic process can be applied to enhancing the performances of other transparent conductors, such as carbon nanotubes, metal oxides, and graphenes.

1. Introduction

Transparent conductors (TCs) are an indispensable component of optoelectronic devices, such as flat panel displays, organic solar cells, organic light-emitting diodes, and touch panels. Indium tin oxide (ITO) has dominated the TC industry due to its excellent optoelectrical performance and technological maturity. The advent of next-generation flexible optoelectronics, however, has necessitated the development of alternatives to the brittle and expensive ITO, which has boosted research into new types of TCs that display good mechanical flexibility while maintaining a low sheet resistance (R_s) and a high optical transmittance (T).[1] Currently, Ag nanowire (NW) TCs constructed from random networks of NWs are regarded as the most appealing new TC because they exhibit better R_s–T performance than other alternatives to ITO, such as carbon nanotubes, graphene, or conducting polymers.[2–5] To achieve optoelectrical properties comparable to those of ITO, it is clear that Ag NW networks must have $R_s \approx 10$ Ω sq^{-1} for $T \geq 90\%$. Such values have not yet been reached through the normal nanostructures of Ag NWs, except in the recently reported Ag NW networks prepared by spin-coating of Cambrios ClearOhm inks.[2,4]

Several groups have systematically examined the performances of Ag NW networks. These groups revealed that the performance is correlated with the NW size (diameter and length) and the NW–NW junction resistance.[6–9] De et al.[7] suggested that thinner NWs or a lower junction resistance could increase the percolative figure of merit (FoM), $\prod$, and the NW diameter should not exceed 20 nm to ensure that $R_s \leq 10$ Ω sq^{-1} at $T = 90\%$. Mutiso et al.[9] showed that a higher NW aspect ratio could reduce the value of R_s at a given T. The aspect ratio of NWs with a diameter of 40 nm and a junction resistance of 2 kΩ should exceed 800 to obtain a value of $R_s \leq 10$ Ω sq^{-1} at $T = 90\%$. That is, the percolation conduction in NW networks characterized by $T \approx 90\%$ is typically governed by the distribution of junction resistance, which, in turn, is dominated by the dimensions of NWs and the concentration of insulating surface ligands.

The degradation of the R_s–T performance as a result of high junction resistances may be mitigated via two different approaches. First, the NW synthesis may be modified to elongate the NWs for the purpose of lowering the areal distribution of NW-NW junctions. Lee et al.[3] synthesized 500 μm long Ag NWs and fabricated the NW networks that displayed $R_s = 9$ Ω sq^{-1} with $T_{@550nm} = 89\%$. Such synthesis process, however, tends to be quite complicated and time-consuming. A second approach involves constructing hybrid structures using metal oxides (ZnO, Al-doped ZnO, TiO_2, and ITO)[10–13]

D. Y. Choi, Y. S. Oh, Prof. H. J. Sung, Prof. S. S. Kim
Department of Mechanical Engineering
Korea Advanced Institute of
Science and Technology (KAIST)
291 Daehak-ro, Yuseong-gu, Daejeon
305-701, South Korea
E-mail: hjsung@kaist.ac.kr; sskim@kaist.ac.kr
Dr. D. Han, Prof. S. Yoo
Department of Electrical Engineering
Korea Advanced Institute of Science and Technology (KAIST)
291 Daehak-ro, Yuseong-gu, Daejeon 305-701, South Korea

DOI: 10.1002/adfm.201500677

or graphenes.[14,15] The application of an overcoated metal oxide or graphene layer is beneficial for decreasing the NW–NW junction resistances with little detriment to T. The hybrid structures containing metal oxides, however, showed a limited flexibility, and those involving graphenes displayed a relatively high R_s (20–30 Ω sq^{-1}) with $T_{@550nm} \approx 90\%$. Hsu et al.[16] demonstrated that it is possible to improve the conductivity of the NW networks by integrating an array of mesoscale Cu wires. In this hybrid structure, the improvement of overall performance was attributed to the high conductivity of the mesoscale metal wires, rather than by reductions in the NW–NW junction resistances; the hybrid conductor displayed an extremely low R_s value of 0.36 Ω sq^{-1} at a T of 92%. The mesoscale Cu wires, however, were generated by depositing thermally evaporated Cu onto electrospun polymer scaffolds. The fabrication process, therefore, was not simple and cost-effective.

Recently, celebrated research groups have reported techniques for manufacturing TCs comprised of patterned metal networks, including microsphere lithography,[17] grain boundary lithography,[18] and selective laser sintering method.[19] The lithographic methods have the ability to fabricate nano-sized metal patterns with a high-resolution, however, they require etching and evaporative deposition steps. The laser sintering method is fast and simple, whereas it inevitably produces a large amount of material waste.

Here, we introduce a hybrid structure composed of a highly conductive ordered array of Ag nanoparticle wires (NPWs) incorporated into a random network of Ag NWs, yielding a R_s below 10 Ω sq^{-1} while maintaining a $T_{@550nm} \geq 90\%$. The NPW arrays were realized using the nonlithographic process based on the well-known "coffee-ring" phenomenon; particles are organized at the three-phase contact line via the capillarity and convective motion in an evaporating meniscus. Each NPW was a few micrometers wide (<10 μm) and was constructed with close-packed nanoparticles which facilitated a high electrical conductivity. The sintered metal networks composed of NPWs and NWs were successfully transferred to a transparent polymer matrix, which addressed significant morphological issues and simultaneously enhanced the electromechanical stability. A computational model was developed for predicting the geometrical sizes of NPWs. We first estimated the R_s–T performance of the NPW arrays, and demonstrated their effect on the improvement in the properties of the NW networks. We showed that the maximum Haacke FoM of the NW networks was considerably enhanced from 0.0260 to 0.0407 Ω^{-1} upon integration with the NPW array. The highly conductive NPW arrays formed via convective self-assembly are expected to provide a simple and cost-effective strategy for enhancing the performances of other TCs.

2. Results and Discussion

2.1. Fabrication of Embedded Ag NPW–NW Hybrid Conductors

2.1.1. Preparation of Ag NPW–NW Hybrid Conductors

A schematic diagram of the procedures used to fabricate the Ag NPW–NW hybrid conductors is given in **Figure 1**a. The overall process consisted of four distinct steps: (i) generation of an ordered NPW array via convective self-assembly; (ii) sintering of the NPW array; (iii) formation of Ag NW networks on the sintered NPW array; and (iv) sintering of the NPW–NW hybrid conductor. In the first step, the NPW array was generated through a convective self-assembly process. As a colloid suspension was injected between two hydrophilic plates, a capillary bridge formed and was confined by capillary forces. An outward solvent flux by evaporation led to the transfer and deposition of particles toward the contact line.[20–25] Self-organization of particles is governed by the attractive capillary forces induced from the menisci formed around particles and the convective migration of particles to ordered structures.[20] The mechanism underlying the convective self-assembly process will be treated in detail in Section 2.2.1. A NPW was formed during the deposition time (t_d), when the substrate was stationary. The next NPW was patterned after the substrate shifted by a controlled distance. As the meniscus was elongated during the translation, the contact angle decreased below the critical receding contact angle. Consequently, the capillary force exceeded the pinning force, and the contact line slipped to a new position.[23–25] The spacing between neighboring NPWs was determined by the product of the moving time (t_m) and moving velocity (v_m) of the substrate. These enforced stick-slip motion of the meniscus repeated periodically to create highly ordered NPW arrays. Unlike the steps used to fabricate the NPW array, the NWs were coated onto the NPW array under continuous substrate motion at $v_m = 100$ μm s^{-1}.

Figure 1b shows optical microscope images of the NPW arrays fabricated from the citrate-stabilized Ag colloids with different concentrations of a nonionic surfactant, polyethylene glycol mono-4-nonylphenyl ether. The particle volume fraction (ϕ) was fixed at 4×10^{-5} v/v in most experiments. The deposition time of 60 s and spacing of 100 μm were applied. An O_2 plasma treatment was conducted on the substrate to increase hydrophilicity, and to generate negative surface charges since the coulombic repulsion between particles and the substrate surface suppresses uniform deposition of particles.[26] As the convective self-assembly progressed, loosely packed or randomly aggregated particles were gradually formed when surfactant-free Ag colloid was used, as shown in Figure 1b(i). The colloidal stability slowly deteriorated under ambient conditions, which increased the tendency to form aggregated or undesirably stuck particles on the substrate. Well-ordered particle structures were obtained upon the addition of proper concentrations of the surfactant to the colloid. The surfactant molecules reinforced the dispersion stability of particles by introducing the steric effects, i.e., the decrease of the particle sticking probability.[27] The critical micelle concentration (CMC) of this surfactant was approximately 1.4×10^{-4} mol L^{-1}.[28] As shown in Figure 1b(iii), the particle ordering was significantly improved at surfactant concentrations of 2.8×10^{-5}–6.3×10^{-5} mol L^{-1}; well-organized particle arrays could be fabricated over a length of several centimeters. Beyond the CMC, however, loosely packed or irregular particle arrays formed due to a pronounced surfactant-driven Marangoni flow, which prevented particles from moving toward the contact line (see the magnified microscope images in Figure S1, Supporting Information).[29] Figure 1c shows an

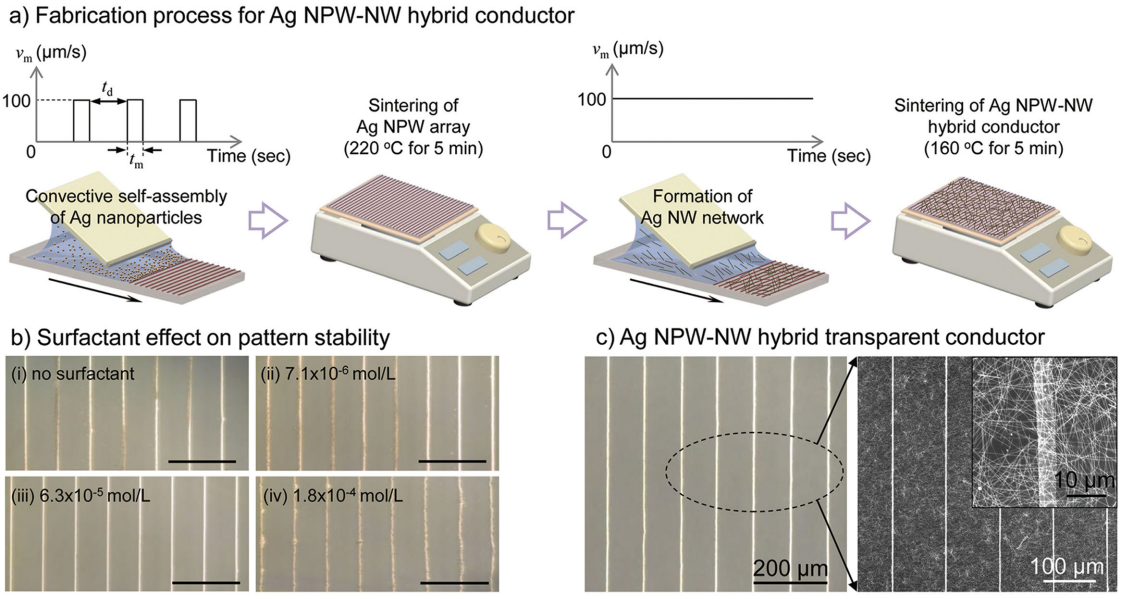

Figure 1. Fabrication of the Ag NPW–NW hybrid conductors. a) Schematic illustration of the procedure used to fabricate the Ag NPW–NW hybrid transparent conductors. t_d is the deposition time for the formation of a NPW. t_m and v_m are the moving time and moving speed of the substrate, respectively. b) Optical microscope images of the NPW arrays fabricated from Ag colloids prepared with different concentrations of the surfactant. Each NPW was generated sequentially from right to left. (Scale bars correspond to 200 μm.) c) Optical microscope image (left) and SEM image (right) of the hybrid conductor, showing that all NPWs remained intact, even after the deposition of the NWs. The inset shows a magnified SEM image of the NWs randomly deposited across a NPW.

Ag NPW–NW hybrid conductor of which NPW arrays were prepared from colloidal Ag nanoparticles stabilized by 6.3×10^{-5} mol L^{-1} of the surfactant. These results indicated that well-ordered NPW arrays could be formed successfully, and it remained intact even after deposition of the NWs. Figure S2, Supporting Information, shows a result of thermal gravimetric analysis (TGA) of the surfactant. The surfactant begins to vaporize at around 200 °C which is less than the sintering temperature (220 °C) of the Ag nanoparticles. The most of surfactant molecules surrounding particles can be eliminated during the sintering process.

2.1.2. Embedding of Ag NPW–NW Hybrid Conductors

The rough surface of the NW networks triggers short circuits in the devices,[1,2,5] moreover the large height of the NPWs can aggravate this issue. The surface morphology of the hybrid conductor was improved for the compatibility with the devices. The rough surface of the hybrid conductor was significantly flattened via embedding of the NPWs and NWs into a transparent polymer matrix. **Figure 2**a illustrates the process to fabricate embedded NPW–NW hybrid conductors. We utilized a commercial Norland Optical Adhesive (NOA) 63 as the polymer matrix, because this material is a clear and colorless liquid photopolymer displaying an excellent optical transparency in the wide spectral range (visible and near-infrared) and a superior mechanical flexibility.[30] The NOA 63 photopolymer was spin-coated onto the sintered hybrid conductors and then cured by exposure to UV light. Following the curing step, the embedded hybrid conductors were peeled off from the glass substrate, and the film thickness was found to be about 100 μm. Unlike the NWs, most of the NPWs were not fully transferred into the surface of NOA 63. Since the adhesion force between the glass and NOA 63 surfaces was rather strong, large strains were unavoidably introduced over the NOA 63 surface during the peeling-off step, which led to just transfers of disconnected or cracked NPWs. To reduce the adhesive strength (or wettability) between these materials, a self-assembled monolayer of fluorinated silanes was deposited on the glass surface prior to the spin-coating of NOA 63.[31] The glass/metal/NOA 63 was immersed in water to further relieve stresses while the cured NOA 63 was detached from the glass substrate; a capillary action of water intervening between the glass and NOA 63 surfaces is helpful in diminishing the mechanical stresses and strains experienced during the peeling-off.[32,33] Through two additional procedures, both NPWs and NWs could be reliably transferred into the NOA 63 surface.

The photograph shown in Figure 2b(i) reveals that the embedded hybrid conductor was flexible and sufficiently transparent that the logos could be viewed below the conductor. Scanning electron microscope (SEM) images of the embedded hybrid conductors are shown in Figure 2b(ii), (iii). These results show that the NPWs and NWs were completely embedded within the NOA 63 surface with the preservation of their integrity. Figure 2c shows an atomic force microscope (AFM) image of the hybrid conductor. The embedded hybrid conductor exhibited an exceptionally smooth surface with a root-mean-square surface roughness of ≈2 nm and a maximum peak-to-valley value of ≈17 nm, indicating that the openings in the metal network of the NPWs and NWs were totally filled with the NOA 63.

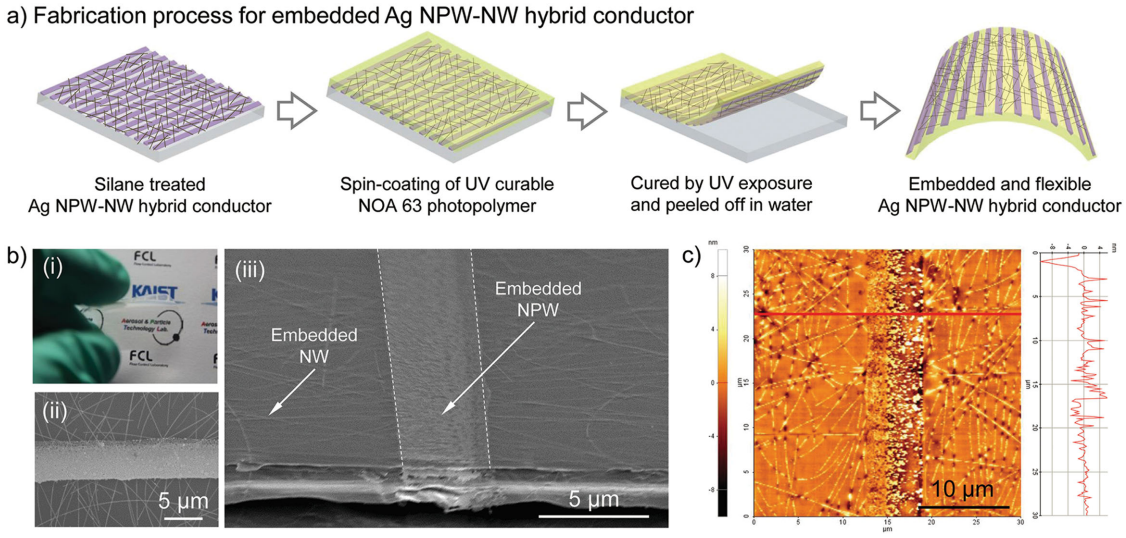

Figure 2. Fabrication of the embedded NPW–NW hybrid conductors. a) Schematic diagram of the procedure used to fabricate the embedded Ag NPW–NW hybrid conductors. b-i) A photograph of the hybrid conductor embedded in a NOA 63 film, indicating good flexibility and transparency. b-ii) Top-view SEM image of the embedded hybrid conductor. b-iii) Angled cross-sectional SEM image of the embedded hybrid conductor. SEM images manifest that the NPWs and NWs were well-embedded in the NOA 63 polymer matrix without destroying their interconnections. c) Topographic AFM image of the embedded hybrid conductor. The right graph shows the contour profile of the embedded hybrid conductor along the red line. The root-mean-square roughness and peak-to-valley values are 2.2 and 17 nm, respectively.

2.2. Characteristics of NPWs

2.2.1. Simple Modeling on the Formation of NPWs

Figure 3a shows a sketch of the mechanism underlying the particle array formation. When a solvent contacts with the solid surface, the contact line of the liquid–solid–air interface is pinned by the wetting hysteresis arisen from the chemical heterogeneity or surface roughness of the solid surface.[34] The pinned contact line results in an outward fluid flow that replenishes the evaporative losses and carries the dispersed particles to the contact line.[21,22,35,36] The particle ordering starts to occur as the particles are pushed toward the solid surface by the deformed air–liquid interface whose height is similar to the particle diameter. These menisci formed around the particles produced a strong long-range interparticle capillary force: the immersion capillary force.[20] The attractive capillary forces pull the particles into an organized structure. Once the particles are assembled, the ordered structures continue to grow with the addition of incoming particles carried by the evaporation-induced capillary flow. Dimitrov et al.[37] proposed a novel approach for estimating the growth rate of an array based on the material mass flux balance at the growth front of a particle array. The growth rate of an array, v_c, may be expressed as

$$v_c = \frac{\beta l j_e \varphi}{h(1-\varepsilon)(1-\varphi)} \tag{1}$$

where β is a coefficient that relates the mean solvent velocity to the mean particle velocity. This value varies from 0 to 1, depending on the strength of the particle–particle and particle–substrate interactions. j_e is the evaporation flux from a pure solvent surface per unit length, l is the evaporation length, and h and ε are the height and porosity of the particle layers, respectively. Here, v_c was derived under the condition that the substrate is withdrawn at the same rate of the array growth.

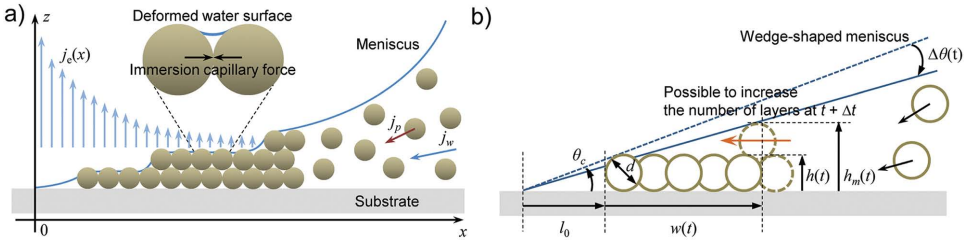

Figure 3. Mechanism on the formation of particle arrays via convective self-assembly. a) Schematic diagram of the particle arrays organized in the vicinity of a contact line. Evaporation induces a compensating water flow which transports the particles toward the contact line. Here, j_w is the water flux, j_p is the particle flux, and j_e is the evaporation flux. b) Illustration of our proposed model for predicting the width and height of hexagonal close-packed layers as a function of the deposition time t. The meniscus was considered to be pinned and constantly thinned over time. Both the width (w) and height (h) of the particle arrays at time, $t + \Delta t$, were calculated using Equation (1) coupled with the number of layers determined from the relationship between the height of the meniscus (h_m) and the height of the particle arrays at t. Here, θ_c is the initial contact angle of the meniscus, l_0 is the location at which self-ordering commences, d is the diameter of particles.

In the steady state, the total evaporation flux, J_{evap}, from a wet particle film is equal to the water flux from the bulk suspension to the ordered particle array, J_w; that is, $J_w = J_{evap}$. In this case, $h_m j_w = l j_e$, where $J_w = h_m j_w$ and $J_{evap} = l j_e$. Here, h_m is the meniscus height above the substrate at the growth front of the array and j_w is the replenishing water flux per unit area. Under these conditions, the absolute position of the growth front is invariant, and the total evaporation flux remains constant during the process. Particle ordering under static conditions, in which neither the substrate nor the meniscus is pulled, is characterized by the shift of the growth front from the contact line toward the bulk suspension over time. In such circumstances, v_c is difficult to estimate because J_{evap}, J_w, and v_c change depending on the location of the growth front and are correlated with one another. Several researchers have used the parameter v_c to fit the measured width of the particle arrays formed under static conditions. They showed experimentally that J_{evap} remains nearly constant and depends only on the temperature and relative humidity.[38,39] In a sessile droplet, the evaporation flux is given by $J_s \propto (R-r)^{-\lambda}$, where $\lambda = (\pi - 2\theta_c)/(2\pi - 2\theta_c)$. Here, R is the droplet radius, r is the radial coordinate, and θ_c is the contact angle.[21] The evaporation flux becomes singular at the perimeter, which induces much enhanced outward flow to compensate for the evaporation loss. Usually, the evaporation process proceeds in a quasi-steady state, except near supercritical conditions.[22,35,36] By the analogy to the droplet, we made two auxiliary assumptions for modeling the particle array growth: 1) the total evaporation flux from the wet particle film, J_{evap}, remained nearly constant because it was dominated by the strong evaporation flux at the contact line, and 2) the overall evaporation was a steady-state process.

To estimate the array growth rate, v_c, the information about the number of layers and the type of crystalline structures in the particle array should be known beforehand. The ordered structures of spherical particles are composed of sequentially stacked layers as: 1Δ, 2□, 2Δ, 3□, 3Δ, ..., where the number denotes the number of layers and the symbols indicates hexagonal (Δ) or square (□) packing of the particles.[20,40] The number of layers depends strongly on the meniscus shape, that is, the contact angle and curvature.[20,41] We successfully evaluated the v_c by considering that the particles are organized in a hexagonal close-packed structure and the number of layers is restricted by the meniscus height. As shown in Figure 3b, the meniscus is thought to be pinned, and be thinning involving a linear decrease in the contact angle by the constant evaporation rate. These conditions are consistent with previous theoretical and experimental studies, which showed that the height and contact angle of the drying droplets decreased roughly linearly during the evaporation.[22,35,36] Additionally, the form of meniscus may be simplified to a wedge shape since the width of a particle array was typically much smaller than 100 μm. The particle ordering begins at a distance, l_0, from the contact line. At this position, the particles touch both air–liquid interface and solid surface, and they are pressed together by the immersion capillary forces.[20] The number of layers (k) at time, t, was determined from the geometric boundary conditions defined by the height of the hexagonal close-packed particles (h) and the meniscus (h_m) at the growth front of an array (see Figure S3, Supporting Information). After v_c was updated with the estimation of k, the width of a particle array (w) was calculated by integrating the v_c over t.

2.2.2. Geometric and R_s–T Properties of NPWs

Figure 4a,b shows the calculated and measured sizes of the particle arrays. The calculations were conducted using two fitting parameters: 0.04 rad of the initial contact angle (θ_c) and 3.5×10^{-5} rad s^{-1} for the decreasing rate of contact angle ($\dot{\theta}$). These graphs revealed that the proposed model predicted very similar widths and heights compared to those evaluated from the AFM analysis, without any advanced knowledge of the thickness or number of layers in the particle arrays. The particle arrays grew monotonically over time, and their widths and heights increased to 6.5 μm and 270 nm, respectively, over a deposition time of 60 s. The smallest width (≈3 μm) was obtained at

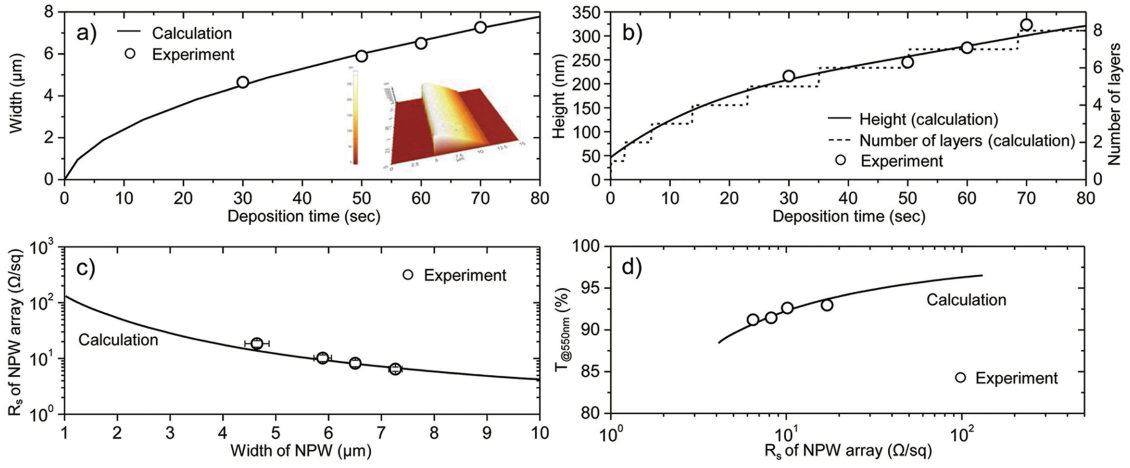

Figure 4. a) The width of the Ag nanoparticle arrays obtained from AFM analysis (circle) and the model calculation (solid line). The inset shows an AFM image of the Ag nanoparticle array. b) Results of the measured height (circle), as well as the calculated height (solid line) and number of layers (dash line). c) Sheet resistance (R_s) of the Ag NPW array versus width of the NPW. d) Plot of the specular transmittance (T) at 550 nm as a function of the R_s of the NPW array. c,d) Each NPW array was fabricated under conditions: spacing of 100 μm and deposition time of 30, 50, 60, or 70 s.

the deposition time of 15 s. We attempted to verify the model by fitting the results to the published data obtained from other particle systems (see Figures S4 and S5, Supporting Information).[38,39] These efforts revealed good agreement between the experimental and theoretical results.

The R_s and T of the NPW arrays could be calculated based on the (averaged) geometrical sizes of the particle patterns, including the width and height. Figure 4c shows R_s of the NPW arrays at different widths of the wire patterns. The results were compared with the data calculated using the following relation

$$R_s = \frac{2\rho}{d+h}\frac{w+s}{w} \tag{2}$$

where ρ is the resistivity of the NPWs, w(h) is the width (height) of a single NPW, d is the mean diameter of the particles, and s is the spacing between neighboring NPWs. The cross-section shape of NPWs was treated as a trapezoid, and the programmed spacing of each NPW was 100 μm. The resistivity of the assembled particle arrays was found to be 5 times higher than that of bulk silver (ρ_B = 1.59 μΩ cm), as determined by fitting Equation (2) to the measured R_s values. Note that the resistivity was determined on the basis of the sizes of unsintered NPWs.

The curve corresponding the R_s–T performances of the NPW arrays is shown in Figure 4d. The optical transmittance was calculated by considering a geometrical shadow loss

$$T = k_1\frac{s}{s+w}\times 100\% \tag{3}$$

The fitting parameter k_1 accounts for the mismatch between the programmed and actual spacing. A fit of Equation (3) to the data presented in Figure 4d gave k_1 = 0.975. The values of R_s and T for the curves shown in Figure 4c,d were calculated according to the values of w and h obtained from the above-mentioned model. The simulation results indicate that the NPW arrays can have a remarkable optoelectrical property with R_s = 5 Ω sq^{-1} at T = 90%. These predictions also suggest that the R_s–T performance is obviously better than that of ITO on film, and the electrical conductivity of the Ag NW networks can be improved if they are hybridized with the NPW arrays. Actually, the NPW arrays exhibited a R_s of 6.4 Ω sq^{-1} at $T_{@550nm}$ = 91% under conditions involving a deposition time of 70 s and a spacing of 100 μm. The mean width of a single wire was approximately 7.3 μm.

2.3. R_s–T Performance of the NPW–NW Conductors

The R_s–T performances of the NW networks and NPW–NW hybrid conductors are depicted in **Figure 5**a. The efficacy of the NPW arrays in improving the optoelectrical properties of the NW networks was examined by comparing the performances of the NPW–NW hybrid conductors to those obtained from the NW networks. In general, the optoelectrical properties of nanostructured metallic thin films are described using R_s and T as follows[42]

$$T = \left(1+\frac{Z_0}{2R_s}\frac{\sigma_{Op}}{\sigma_{DC,B}}\right)^{-2} \tag{4}$$

where Z_0 is the impedance of free space (377 Ω), σ_{Op} is the optical conductivity, and $\sigma_{DC,B}$ is the bulk DC conductivity of the film. The term $\sigma_{DC,B}/\sigma_{Op}$ is often used as a bulk-like FoM, and its higher value represents a better performance of the TCs. Recently, De et al.[7] proposed a modified expression of Equation (4) to account for the discrepancies between the predicted and experimentally measured R_s–T performances in very thin films due to percolation effects

$$T = \left[1+\frac{1}{\Pi}\left(\frac{Z_0}{R_s}\right)^{1/(n+1)}\right]^{-2} \tag{5}$$

where $\prod$ is a percolative FoM and n is a percolation exponent. A low R_s coupled with a high T leads to a large value of $\prod$. The bulk like and percolative FoMs of the Ag NW networks were obtained by fitting the experimental results to Equations (4) and (5), respectively. The fitted results gave $\sigma_{DC,B}/\sigma_{Op}$ = 260, $\prod$ = 137.9, and n = 0.64. The NPW arrays applied to the hybrid conductors were generated under a deposition time of 60 s and a programmed spacing of 200 μm. The NPWs showed a mean value of 6.5 μm in width and 270 nm in height prior to sintering. The NW networks with various areal densities were overcoated onto the sintered NPW arrays. The hybrid conductors showed lower values of R_s than those of the NW networks at the same $T_{@550nm}$. The values of R_s for the NW networks in the percolative regime decreased significantly upon integration with the NPW arrays, displaying a 3%–4% loss in $T_{@550nm}$. From the supposition that a NPW array and a NW network are electrically connected in parallel, the resultant resistance of the hybrid conductor can be simply expressed as $R_{s,hy} = (1/R_{s,NPW} + 1/R_{s,NW})^{-1}$, where $R_{s,NPW}$ and $R_{s,NW}$ denote R_s of a NPW array and a NW network, respectively. The final T value of the hybrid conductor is just the multiplication between the respective T of the NPW array and the NW network, that is, $T_{hy} = T_{NPW}T_{NW}$. In a nanobundle thin-film transistor, the current can be expressed by a scaling formula, $I_D \approx (1/L_S)(L_S/L_C)^m$, where L_S is the stick length, L_C is the channel length between the source and drain, and m is the universal exponent of the stick percolating system.[43,44] For example, near the percolation threshold ($\rho_{th} = 4.236^2/\pi L_s^2$), $m \approx 1.8$.[44] At a given ρ_S (or given m), I_D increases with decreasing L_C due to the increased probability of sticks to connect the source and drain.[43] In the hybrid conductor, the electrical properties of the NW networks in the percolative regime could be enhanced since the newly formed NW–NPW–NW paths improved the overall connections in the NW networks. We did not use Equation (5), but Equation (4), to express T_{NW} as a function of $R_{s,NW}$ in the hybrid conductor. The relationship between T_{hy} and $R_{s,hy}$ could be derived as follows

$$T_{hy} = k_1k_2\frac{s}{w+s}\left[1+\frac{Z_0}{2}\frac{\sigma_{Op}}{\sigma_{DC,B}}\left(\frac{1}{R_{s,hy}}-\frac{(d+h)w}{2\rho(w+s)}\right)\right]^{-2} \tag{6}$$

where the fitting parameter k_2 accounts for the reduction in T loss as a result of the NWs overlapped onto NPWs. A fit of

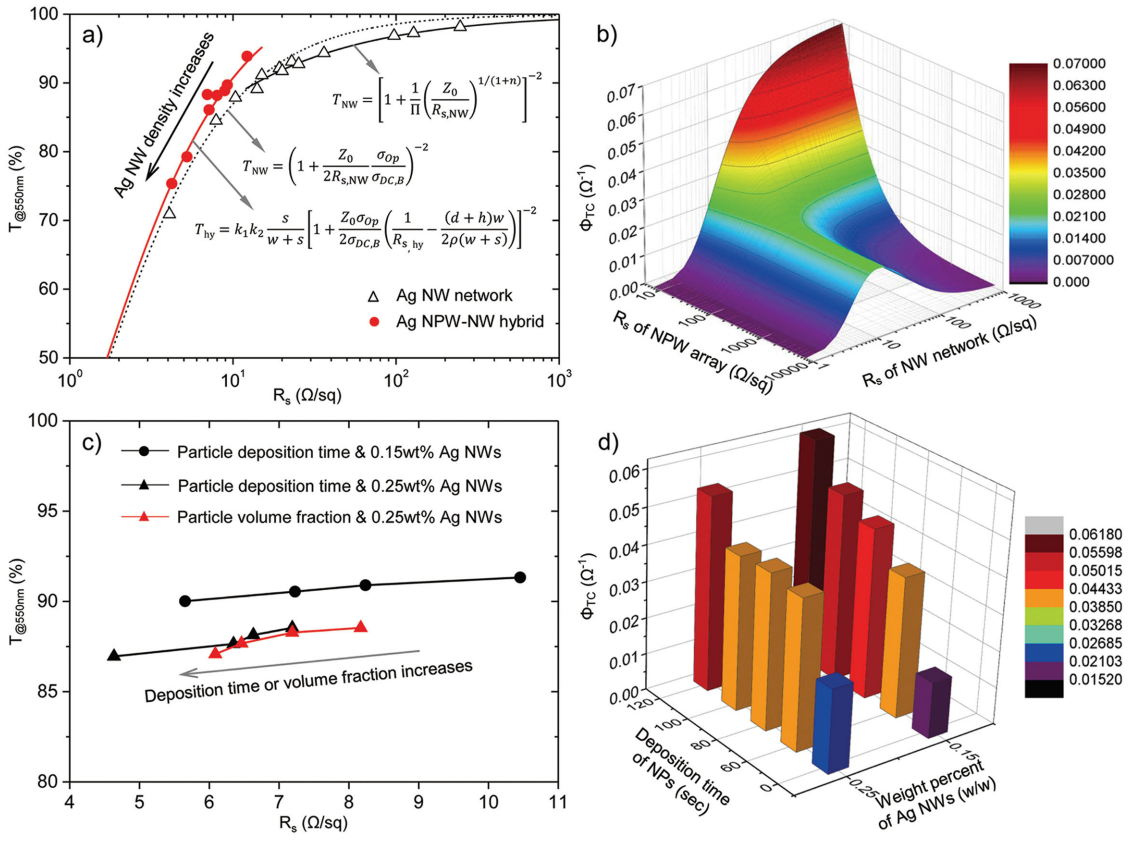

Figure 5. a) The R_s–T performances of the Ag NPW–NW hybrid conductors and Ag NW networks. Each NPW array used in the hybrid conductors was generated under conditions: spacing of 200 μm and deposition time of 60 s. b) A 3D plot of simulated $_{TC}$ ($=T^{10}/R_s$) for the hybrid conductors at various combinations of the NPW arrays and NW networks. c) Specular T at 550 nm as a function of the R_s of the NPW–NW hybrid conductor. The NPWs constructing each NPW array were generated under conditions: spacing of 200 μm and deposition time of 60, 80, 100, or 120 s. The particle volume fraction of the Ag colloid was modified to 3×10^{-5}, 4×10^{-5}, 5×10^{-5}, or 6×10^{-5} v/v, and the weight percent of the NW suspension was adjusted to 0.15 or 0.25 w/w. d) Bar graph showing the $_{TC}$ obtained from the NPW–NW hybrid conductors fabricated under above conditions.

Equation (6) to the experimental results obtained from the hybrid conductors gave $k_2 = 1.01$. Note that this expression is equivalent to Equation (4) when $w = 0$ or $s \to \infty$, as expected, and $R_{s,hy}$ may be applied independently if the physical or geometrical properties of the NPW array remains fixed. As shown in Figure 5a, Equation (6) suggests that the optoelectrical properties of the hybrid conductors gradually shifted toward the corresponding properties of the NW networks as the areal density of NWs increased.

Figure 5b shows the simulated optoelectrical performances of the hybrid conductor prepared from various combinations of the NPW arrays and NW networks. The FoM, ϕ_{TC}, defined by Haacke[45] was used to characterize the performance of the hybrid conductor, $\phi_{TC} = T^{10}/R_s$. The higher value of ϕ_{TC} yields a low value of R_s or a high value of T. In the simulation, the spacing between NPWs was fixed to 200 μm, and the geometrical sizes (w and h) were calculated using the model for array growth. The maximum value of ϕ_{TC} for the NW networks increased considerably from 0.0260 to 0.0407 Ω^{-1} through the integration with the NPW arrays (cf. a conductor with R_s of 10 Ω sq^{-1} at T of 90% shows $\phi_{TC} = 0.0349$ Ω^{-1}). These promising results imply that the NPW arrays ordered via convective self-assembly are capable of providing a simple and cost-effective route to boost the R_s–T performances of the NW networks. We further demonstrated the performance enhancement of the hybrid conductors according to the geometrical size of the NPWs as shown Figure 5c,d. As the size of the NPWs increased, the R_s of the hybrid conductors was rather noticeably decreased than that of T, and therefore the ϕ_{TC} of the hybrid conductors was steadily improved; the R_s of 10.5 Ω sq^{-1} and $T_{@550nm}$ of 91.3% were changed to R_s of 5.7 Ω sq^{-1} and $T_{@550nm}$ of 90% as the deposition time was increased from 60 to 120 s in the hybrid conductors prepared from 0.15 wt% of the NW suspension. The overall property of the hybrid conductors were pronouncedly affected by the optoelectrical property of the NPW arrays when the thinner coated NWs were applied, which was analogous to the trend presented in Figure 5b. We demonstrated that the performance improvement of the NW networks could be achieved by applying the NPW arrays formed from the convective self-assembly. However, the overall process time was a bit long. The process time can be reduced by three strategies: i) reduction of the deposition time by increasing the evaporation rate, which can be accomplished by raising the process temperature or by lowering the relative humidity or by using the highly volatile organic-based colloids; ii) reduction of the deposition time by increasing the particle volume fraction;

iii) one-step fabrication of the NPW and NW networks by using the mixture of NPs and NWs. By utilizing the different surface deformation energy according to the aspect ratio of particles,[46] we would generate the NPW and NW networks simultaneously.

2.4. Long-Term and Electromechanical Stability

The R_s and T values measured from the embedded hybrid conductor were compared with those obtained from a commercial ITO film on a polyethylene terephthalate (PET) substrate, as shown in **Figure 6**a. The measured T values include the effect of substrates. The embedded hybrid conductor showed a R_s of 8.3 Ω sq^{-1} and a $T_{@550nm}$ of 80.5%. The optoelectrical performance of the embedded hybrid conductor was superior to that of the ITO film which displayed a R_s of 14.9 Ω sq^{-1} coupled with a $T_{@550nm}$ of 81.9%. The low R_s of the embedded hybrid conductor revealed that the NPWs did not crack and most of the electrical connections in the hybrid structure remained intact during the entire process. The T values of the hybrid conductor maintained nearly constant in the wavelength range of 350 to 1200 nm, except for the drop in T due to the absorption by surface plasmons on the NWs around 350 nm.[2,30] However, the T values of the ITO film displayed fluctuations over the visible region and decreased rapidly in the UV spectrum.

Long-term stability tests were conducted for the NW conductor, the embedded NW conductor, the NPW–NW conductor and the embedded NPW–NW conductor in air (24 ± 1 °C, 40% ± 2%) as shown in Figure 6b. The normalized resistance change, $\Delta R/R_0$, was used for comparison, where R_0 is the initial resistance and ΔR is the resistance change. After 7 d, the $\Delta R/R_0$ of the NW conductor and of the NPW–NW conductor rapidly increased to 32.9% and 33.4%, respectively. However, the $\Delta R/R_0$ of the embedded NW conductor and of the embedded NPW–NW conductor slowly increased to 4.5% and 4.2%, respectively. The encapsulation of the NPWs and NWs by the NOA polymer matrix significantly improved the oxidation resistance.

In addition, the embedded hybrid conductors exhibited outstanding electromechanical stability, which is increasingly important in the emerging field of flexible electronics. As shown in Figure 6c, the hybrid conductor was bent perpendicular to the longitudinal direction of the NPWs in the bending test. Figure 6d illustrates the distinction between the resistance change of the ITO film and that of the embedded hybrid conductors, as a function of the bending cycle. The conductors were bent to a bending radius of 4 mm, and the resistance measurements were collected after the film was reflattened. The resistance of the ITO film increased sharply after just a few bending cycles, and numerous visible fine cracks formed. In stark contrast, the embedded hybrid conductors displayed excellent bending fatigue strength. The resistances of the embedded hybrid conductors remained similar to their original values, even after 1000 bending cycles; the values of $\Delta R/R_0$ were 0.14 and 0.24 under tensile and compressive stresses, respectively. Figure 6e shows the changes in the resistance of the embedded hybrid conductor at different bending radii. $\Delta R/R_0$ increased slightly less than 0.15 as the embedded hybrid conductor was bent up to a 3 mm in bending radius. Even though the bending radius became approximately 500 µm, it showed a relatively good conductivity corresponding to $\Delta R/R_0 \approx 1.0$. The superior

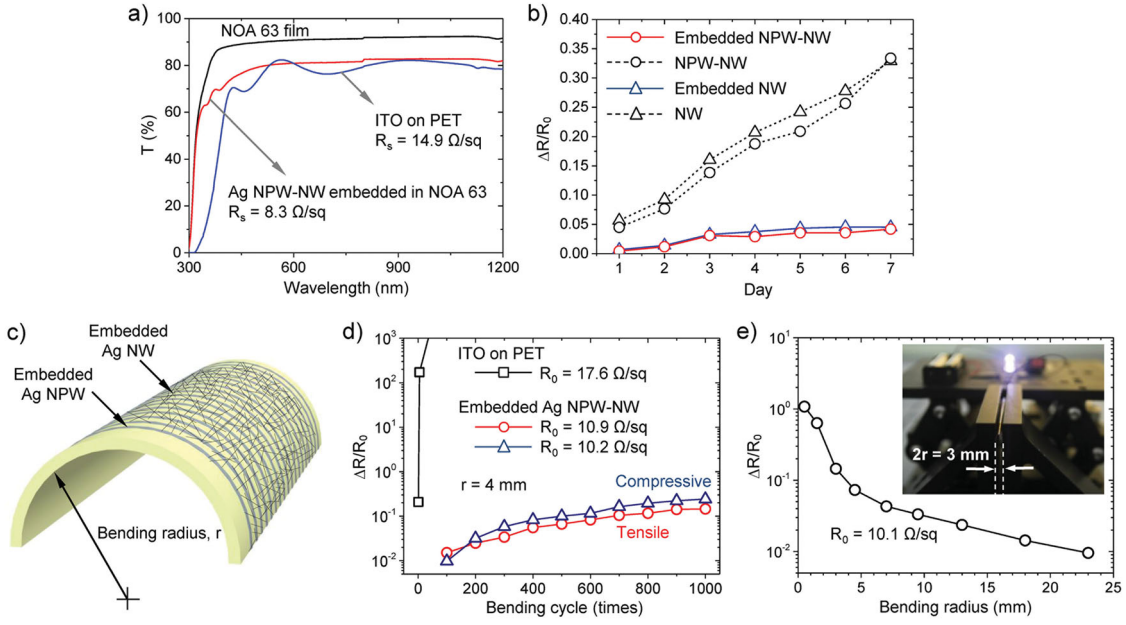

Figure 6. a) Specular transmittance spectra measured over the wavelength range 300–1200 nm: 100 µm thick NOA 63 film (black), Ag NPW–NW hybrid conductor embedded in the NOA 63 (red), ITO on PET (blue). b) The resistance change of the NW, embedded NW, NPW–NW, and embedded NPW–NW conductors with the exposure time to air. c) Schematic diagram of the bended hybrid conductor. d) Plot of the normalized resistance change in the ITO on PET and the embedded hybrid conductors over bending cycles at a bending radius of 4 mm. e) Plot of the normalized resistance change in the embedded hybrid conductor as a function of the bending radius. The inset shows a photograph of the illuminated LED lamp mounted on the embedded hybrid conductor bent with a bending radius of 1.5 mm.

electromechanical stability was attributed to the strong adhesion between the NOA 63 and the metal networks, which helped to preserve electrical contacts under extreme bending stresses.[30] The mechanical adhesion between the NPW (or NW) and NOA film was evaluated by using the adhesive tape as shown in Figure S6, Supporting Information. After five times of tape peeling, the resistance maintained its initial value of ≈12 Ω.

2.5. Application to Organic Solar Cells

To verify the enhancement of electrical conduction through the NPW arrays in flexible electronic devices, the NPW–NW hybrid conductors were applied to a flexible organic solar cell (OSC) as an anode electrode. **Figure 7** shows the current density–voltage (J–V) characteristics of the flexible OSCs fabricated using the embedded Ag NPW–NW hybrid conductor (R_s of 8.7 Ω sq^{-1} with $T_{@550nm}$ of 81%) and embedded Ag NW network (R_s of 16.6 Ω sq^{-1} with $T_{@550nm}$ of 85%). An ITO on glass (R_s of 20 Ω sq^{-1} with $T_{@550nm}$ of 88%) was used as a reference. All T values of these conductors include the light absorption of the substrate. A blend of thieno[3,4-*b*]thiophene/benzodithiophene (PTB7) and [6,6]-phenyl C71-butyric acid methyl ester (PC71BM) was used as the photoactive layer in the devices. The NPW–NW OSC had a short-circuit current density (J_{sc}) of 12.1 mA/cm^2, an open-circuit voltage (V_{oc}) of 0.70 V, and a fill factor (FF) of 35.8%, resulting in a power conversion efficiency (PCE) of 3.1%, which was higher than that of the NW OSC showing a J_{sc} of 11.7 mA cm^{-2}, a V_{oc} of 0.72 V, a FF of 33.3%, and a PCE of 2.8%. The incorporation of the NPW array to the NW network results in higher FF and PCE values due to the decrease in R_s value.[31] The charge transport became more efficient by the NPWs providing the low resistive paths, which improved the FF.[47] However, the PCE of the NPW–NW OSC or the NW OSC was inferior to that of the ITO OSC in Figure 7. The ITO OSC exhibited a J_{sc} of 14.0 mA cm^{-2}, a V_{oc} of 0.73 V, and a FF of 69.4%, resulting in a PCE of 7.1%. The primary reason for the lower PCE and FF values of NOA-based OSC was the low thermal stability of the NOA film. Since the NOA film was easily crumpled by the heat treatment during device fabrication, the electrical property and surface morphology of the embedded conductors were deteriorated.

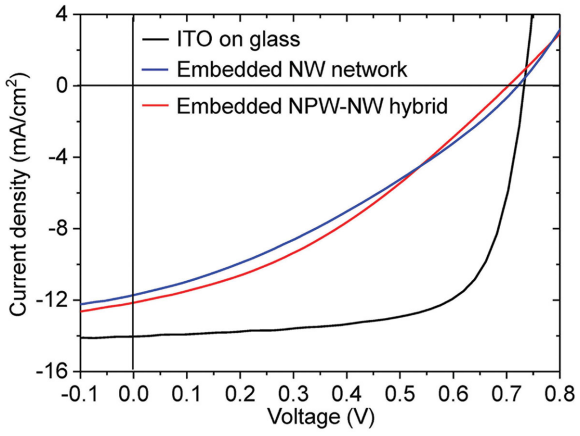

Figure 7. Current density versus voltage.

3. Conclusion

We fabricated stable and well-organized Ag NPW arrays via convective self-assembly which is a simple, cost-effective and nonlithographic method by adding a nonionic surfactant to the Ag colloids. The surfactant enhanced the colloidal stability enough to maintain the self-ordering property of the Ag nanoparticles. The morphological and electromechanical characteristics of the hybrid conductors were considerably improved by embedding the NPWs and NWs into transparent UV curable photopolymer, NOA 63, through a reliable transfer process complemented by the two key strategies: increasing the hydrophobicity of substrates and the capillary action of water during the peeling-off. Furthermore, the R_s–T performances of the NPW arrays were successfully estimated based on the geometrical sizes of the NPWs calculated from the array growth model developed in this work. Through the simple model and experimental results, we demonstrated that the NPW arrays could provide a better optoelectrical property than that of ITO films or NW networks. The superior property of the NPW arrays facilitated significant performance enhancements of the NW networks when they were hybridized with the NW networks. Highly conductive NPW arrays generated by the facile process could be utilized in other TC structures, such as carbon nanotubes, metal oxides, conducting polymers, and graphenes, to improve their optoelectrical performances.

4. Experimental Section

Materials: An aqueous suspension of citrate-capped Ag nanoparticles with a diameter of 47 ± 5.0 nm (50 nm Citrate Biopure Silver) was purchased from nanoComposix Co., Ltd. Ag NWs dispersed in deionized water were received from N&B Co., Ltd. The mean length and diameter of the supplied NWs were 20 μm and 40 nm, respectively. Prior to use, each of the Ag colloid and NW suspension was diluted to a desired concentration with deionized water (resistivity = 18.2 MΩ cm). The nonionic surfactant, polyethylene glycol mono-4-nonylphenyl ether, was obtained from Tokyo Chemical Industry Co., Ltd.

Fabrication of the Ag NPW Arrays and the NW Networks: Cover glasses with dimension of 24 × 40 mm^2 (Paul Marienfeld GmbH & Co. KG) were used as substrates. The cover glasses were cleaned successively with acetone, ethanol, and isopropyl alcohol in an ultrasonic bath for 15 min each, followed by drying with nitrogen gas. The cleaned substrates were then treated by an O_2 plasma for 5 min. Each of the NPW arrays and NW networks was fabricated by using a programmable syringe pump (LEGATO 180, kdScientific) equipped with a stainless steel plate as a translation stage. A 3 M scotch tape was attached to the cover glass with leaving about 1 mm from the edge, and they were used as a blade. The blade was installed on an XYZ stage with adjustable rotational alignments, and was tilted at an angle of 30° from the horizontal surface. The blade was contacted with the substrate before 60–80 μL of the suspension was injected into the formed wedge. The blade was then raised to 350 μm above the substrate. Once the capillary bridge of the solution had formed, the stage was shifted at a velocity of 100 μm s^{-1} after a typical deposition time of 60 s for the formation of the NPW arrays. For coating the NWs, the stage was continuously translated at a velocity of 100 μm s^{-1}. The Ag NPW arrays and NW networks were sintered at 220 and 160 °C for 5 min, respectively. All fabrication

processes were carried out at room temperature (23 ± 0.5 °C) and at a relative humidity of 45% ± 5%.

Fabrication of the Embedded Ag NPW–NW Hybrid Conductor: The substrate surfaces of the sintered hybrid conductors were rendered hydrophobic by depositing self-assembled monolayers in a vacuum chamber for 30 s using 1H, 1H, 2H, 2H-perfluorooctyltrichlorosilane. After the silane surface treatment, NOA 63 photopolymers were spin-coated onto the hybrid conductors at 500 rpm for 40 s. The NOA 63 was cured by exposure to at least 4.5 J sq^{-1} cm^{-1} of UV light (365 nm) at room temperature, and then the cured NOA 63 was carefully peeled away from the glass substrate in a water bath.

Model Simulation: The particle diameter (d) and particle volume fraction (ϕ) were 47 nm and 4×10^{-5} v/v, respectively. $\beta = 1.0$ was applied and the total evaporation flux, $j_e = 308$ μm^2 s^{-1} was determined from the same procedure used by Hanafusa et al.[39] Calculations were conducted with a time step of 10 ms.

Device Fabrication: The OSCs were fabricated on the NPW–NW, NW conductors embedded into NOA 63. An UV/ozone (UV/O_3) treatment was conducted on the embedded conductors for 30 min, and 50 nm thick PEDOT:PSS (PH1000) layer was spin-coated on the embedded conductors, followed by 15 min of annealing at 140 °C in air. After the PEDOT:PSS coated embedded conductors were transferred into a nitrogen-filled glove box, 100 nm thick bulk hetero-junction (BHJ) layer was spin-coated from the solution of PTB7:PC71BM (25 mg mL^{-1}, 1:1.5 w/w) in chlorobenzene:1,8-diidoctane (DIO) (97:3 v/v), dried at 70 °C for 20 min in the glove box, 2,9-dimethyl-4,7 diphenyl-1,10-phenanthroline (BCP) layer (8 nm) and Al layer (100 nm) were sequentially deposited on top of the patterned PTB7:PC71BM layer through a shadow mask by thermal evaporation at 10^{-7} Torr. The active area for all the devices was defined as 15 mm^2 by a shadow mask.

Characterization: All SEM or AFM images were obtained using a scanning electron microscopy (S-4800, HITACHI) or a scanning probe microscopy (XE-100, Park Systems) operated in tapping mode, respectively. The specular transmission spectra were acquired using a UV–Vis–NIR spectrometer (V-570, Jasco), and the sheet resistances were measured using the two-terminal method. For the sheet resistance measurements of the Ag NPW–NW hybrid conductors, two contacts were drawn along the direction perpendicular to the NPWs by a silver pen (CW2200MTP for glass-based conductors or CW2900 for NOA 63-based conductors, ITW Chemtronics), separated by a square area of the conductor, and then the resistance was measured by using the Keithley 4200-SCS. The sheet resistance of the NW conductor was measured using the same procedure for the hybrid conductor. The sheet resistance of the ITO on PET was measured using the four-point probe system (FPP-HS8, DASOLENG). Current density–voltage (J–V) characteristics were obtained under irradiance of 100 mW cm^2 from a 150 W Xe short arc lamp filtered by an AM 1.5 G filter with a solar simulator (PEC-L12, Peccell Technologies).

Supporting Information

Supporting Information is available from the Wiley Online Library or from the author.

Acknowledgements

This work was supported by the Global Leading Technology Program (N02140329) funded by the Ministry of Trade, Industry and Energy, and by the Creative Research Initiatives (No. 2014–001493) program of the National Research Foundation of Korea (MSIP).

Received: February 17, 2015
Revised: April 8, 2015
Published online: May 15, 2015

[1] J.-Y. Lee, S. T. Connor, Y. Cui, P. Peumans, *Nano Lett.* **2008**, *8*, 689.
[2] D.-S. Leem, A. Edwards, M. Faist, J. Nelson, D. D. C. Bradley, J. C. de Mello, *Adv. Mater.* **2011**, *23*, 4371.
[3] J. Lee, P. Lee, H. Lee, D. Lee, S. S. Lee, S. H. Ko, *Nanoscale* **2012**, *4*, 6408.
[4] M. Song, D. S. You, K. Lim, S. Park, S. Jung, C. S. Kim, D.-H. Kim, D.-G. Kim, J.-K. Kim, J. Park, Y.-C. Kang, J. Heo, S.-H. Jin, J. H. Park, J.-W. Kang, *Adv. Funct. Mater.* **2013**, *23*, 4177.
[5] D. Y. Choi, H. W. Kang, H. J. Sung, S. S. Kim, *Nanoscale* **2013**, *5*, 977.
[6] S. De, T. M. Higgins, P. E. Lyons, E. M. Doherty, P. N. Nirmalraj, W. J. Blau, J. J. Boland, J. N. Coleman, *ACS Nano* **2009**, *3*, 1767.
[7] S. De, P. J. King, P. E. Lyons, U. Khan, J. N. Coleman, *ACS Nano* **2010**, *4*, 7064.
[8] S. M. Bergin, Y.-H. Chen, A. R. Rathmell, P. Charbonneau, Z.-Y. Li, B. J. Wiley, *Nanoscale* **2012**, *4*, 1996.
[9] R. M. Mutiso, M. C. Sherrott, A. R. Rathmell, B. J. Wiley, K. I. Winey, *ACS Nano* **2013**, *7*, 7654.
[10] F. S. F. Morgenstern, D. Kabra, S. Massip, T. J. K. Brenner, P. E. Lyons, J. N. Coleman, R. H. Friend, *Appl. Phys. Lett.* **2011**, *99*, 183307.
[11] A. Kim, Y. Won, K. Woo, S. Jeong, J. Moon, *Adv. Funct. Mater.* **2014**, *24*, 2462.
[12] R. Zhu, C.-H. Chung, K. C. Cha, W. Yang, Y. B. Zheng, H. Zhou, T.-B. Song, C.-C. Chen, P. S. Weiss, G. Li, Y. Yang, *ACS Nano* **2011**, *5*, 9877.
[13] C.-H. Chung, T.-B. Song, B. Bob, R. Zhu, Y. Yang, *Nano Res.* **2012**, *5*, 805.
[14] R. Chen, S. R. Das, C. Jeong, M. R. Khan, D. B. Janes, M. A. Alam, *Adv. Funct. Mater.* **2013**, *23*, 5150.
[15] D. Lee, H. Lee, Y. Ahn, Y. Jeong, D.-Y. Lee, Y. Lee, *Nanoscale* **2013**, *5*, 7750.
[16] P.-C. Hsu, S. Wang, H. Wu, V. K. Narasimhan, D. Kong, H. R. Lee, Y. Cui, *Nat. Commun.* **2013**, *4*, 2522.
[17] T. Gao, B. Wang, B. Ding, J.-K. Lee, P. W. Leu, *Nano Lett.* **2014**, *14*, 2105.
[18] C. F. Guo, T. Sun, Q. Liu, Z. Suo, Z. Ren, *Nat. Commun.* **2014**, *5*, 3121.
[19] S. Hong, J. Yeo, G. Kim, D. Kim, H. Lee, J. Kwon, H. Lee, P. Lee, S. H. Ko, *ACS Nano* **2013**, *7*, 5024.
[20] N. D. Denkov, O. D. Velev, P. A. Kralchevsky, I. B. Ivanov, H. Yoshimura, K. Nagayama, *Langmuir* **1992**, *8*, 3183.
[21] R. D. Deegan, O. Bakajin, T. F. Dupont, G. Huber, S. R. Nagel, T. A. Witten, *Nature* **1997**, *389*, 827.
[22] R. D. Deegan, O. Bakajin, T. F. Dupont, G. Huber, S. R. Nagel, T. A. Witten, *Phys. Rev. E* **2000**, *62*, 756.
[23] C. Farcau, H. Moreira, B. Viallet, J. Grisolia, L. Ressier, *ACS Nano* **2010**, *4*, 7275.
[24] H. S. Kim, C. H. Lee, P. K. Sudeep, T. Emrick, A. J. Crosby, *Adv. Mater.* **2010**, *22*, 4600.
[25] J. Lawrence, J. T. Pham, D. Y. Lee, Y. Liu, A. J. Crosby, T. Emrick, *ACS Nano* **2014**, *8*, 1173.
[26] Q. Yan, L. Gao, V. Sharma, Y.-M. Chiang, C. C. Wong, *Langmuir* **2008**, *24*, 11518.
[27] A. Crivoi, F. Duan, *J. Phys. Chem. B* **2013**, *117*, 5932.
[28] S. Watanabe, K. Inukai, S. Mizuta, M. T. Miyahara, *Langmuir* **2009**, *25*, 7287.
[29] T. Still, P. J. Yunker, A. G. Yodh, *Langmuir* **2012**, *28*, 4984.
[30] S. Nam, M. Song, D.-H. Kim, B. Cho, H. M. Lee, J.-D. Kwon, S.-G. Park, K.-S. Nam, Y. Jeong, S.-H. Kwon, Y. C. Park, S.-H. Jin, J.-W. Kang, S. Jo, C. S. Kim, *Sci. Rep.* **2014**, *4*, 4788.
[31] S. Jung, S. Lee, M. Song, D.-G. Kim, D. S. You, J.-K. Kim, C. S. Kim, T.-M. Kim, K.-H. Kim, J.-J. Kim, J.-W. Kang, *Adv. Energy Mater.* **2014**, *4*, 1300474.

[32] Y. Lee, S. Bae, H. Jang, S. Jang, S.-E. Zhu, S. H. Sim, Y. I. Song, B. H. Hong, J.-H. Ahn, *Nano Lett.* **2010**, *10*, 490.
[33] M. Donolato, C. Tollan, J. M. Porro, A. Berger, P. Vavassori, *Adv. Mater.* **2013**, *25*, 623.
[34] M. E. R. Shanahan, *Langmuir* **1995**, *11*, 1041.
[35] B. J. Fischer, *Langmuir* **2002**, *18*, 60.
[36] H. Hu, R. G. Larson, *J. Phys. Chem. B* **2002**, *106*, 1334.
[37] A. S. Dimitrov, K. Nagayama, *Langmuir* **1996**, *12*, 1303.
[38] Y. Mino, S. Watanabe, M. T. Miyahara, *ACS Appl. Mater. Interfaces* **2012**, *4*, 3184.
[39] T. Hanafusa, Y. Mino, S. Watanabe, M. T. Miyahara, *Adv. Powder Technol.* **2014**, *25*, 811.
[40] B. Pansu, P. Pieranski, P. Pieranski, *J. Phys.* **1984**, *45*, 331.
[41] M. H. Kim, S. H. Im, O. O. Park, *Adv. Funct. Mater.* **2005**, *15*, 1329.
[42] M. Dressel, G. Grunner, *Electrodynamics of Solids: Optical Properties of Electrons in Matter*, Cambridge University Press, Cambridge **2002**.
[43] N. Pimparkar, J. Guo, M. A. Alam, *IEEE Trans. Electron Devices* **2007**, *54*, 637.
[44] N. Pimparkar, Q. Cao, S. Kumar, J. Y. Murthy, J. Rogers, M. A. Alam, *IEEE Electron Device Lett.* **2007**, *28*, 157.
[45] G. Haacke, *J. Appl. Phys.* **1976**, *47*, 4086.
[46] P. J. Yunker, T. Still, M. A. Lohr, A. G. Yodh, *Nature* **2011**, *476*, 308.
[47] B. Ray, M. R. Khan, C. Black, M. A. Alam, *IEEE J. Photovolt.* **2013**, *3*, 318.